A critical evaluation of the microstructural gradient along the build direction in electron beam melted Ti-6Al-4V alloy

Sharma, H., Parfitt, D., Syed, A., Wimpenny, D., Muzangaza, E., Baxter, G. & Chen, B.

A critical evaluation of the microstructural gradient along the build direction in electron beam melted Ti-6Al-4V alloy

H. Sharma[a], D. Parfitt[a], A.K. Syed[a], D. Wimpenny[b], E. Muzangaza[b], G. Baxter[c], B. Chen[a,d]*

[a]*Faculty of Engineering, Environment and Computing, Coventry University, Coventry, CV1 5FB, UK*

[b]*The Manufacturing Technology Centre Ltd, Pilot Way, Ansty Park, Coventry, CV7 9JU, UK*

[c]*Rolls Royce plc, Derby, DE24 8BJ, UK*

[d]*The Institute for Advanced Manufacturing and Engineering, Coventry University, Beresford Avenue, Coventry, CV6 5LZ, UK*

*Corresponding author. E-mail address: bo.chen@coventry.ac.uk

Abstract

It is generally recognised that electron beam melted (EBM) Ti-6Al-4V alloys exhibit a microstructural gradient along the build direction, but there have been some inconsistent experimental observations and debate as to the origin and magnitude of this effect. Here we present an unambiguous evaluation of this microstructural gradient and associated mechanical property along the EBM build direction on purpose-built round bar RB samples with build height of 380 mm and rectangular plate RP samples with build height of 120 mm. Columnar prior β grain width was found to increase (from 86±38 to 154±56 μm in RB and from 79±34 to 122±56 μm in RP samples) with the build height and the similar increase was also observed for α lath width (from 0.58±24 to 0.87±33 μm in RB and from 1.50±45 to 1.80±49 μm in RP samples). These observations can be attributed to the thermal gradient in the powder bed that produced a cooling rate gradient along the build height. The measured α lath width variation along the build height followed a log-normal distribution. The graded microstructure resulted in a decrease in micro-hardness which correlated very well with the mean α lath width by following a Hall-Petch relation.

Keywords: Electron beam melting, Additive manufacturing, Graded microstructure, Mechanical property, Titanium

1. Introduction

Ti-6Al-4V alloy possesses a unique combination of high strength, low density, and excellent corrosion resistance in aggressive environments. This alloy is thus attractive for aerospace, automobile and biomedical industries [1]. However, manufacturing high-integrity Ti-6Al-4V parts is not cost-effective due to its low thermal conductivity and high reactivity with oxygen [2]. In recent years, electron beam melting (EBM) process has received attention to produce near net shape parts by depositing successive layers of materials through melting metal powders using a high-energy electron beam [3–7]. Generally, as-EBM Ti-6Al-4V shows a better combination of tensile strength and ductility (e.g. 976 MPa for typical ultimate tensile strength and 15% for elongation to failure) when compared to the selective laser melting (SLM) fabricated (e.g. 1421 MPa and 3.2%) as well as wrought Ti-6Al-4V counterparts (e.g. 933 MPa and 13%) [8]. Furthermore a lower residual stress is obtained in the as-EBM condition due to the high build temperature [9].

During the EBM process, the deposited material undergoes a typical thermal cycle of preheating, melting, rapid solidification and phase transformation. The high thermal gradient along the build direction in as-EBM Ti-6Al-4V results in a columnar prior β grain delineated by grain boundary α-phase [10–14]. During the build process, columnar prior β grains epitaxially grow along the <001> crystallographic orientation which aligns parallel to the build direction. This is mainly due to the large thermal gradient and pseudo-uniaxial heat transfer with directional solidification [14]. Within the prior β grain, the α+β microstructure has been reported with both Widmanstätten (or basketweave) and colony morphology. The prior β-phase was found to be in dot and rod morphology observed in a 2D plane and their volume fraction was typically ~2.7% in the as-EBM condition [13]. The microstructure at the top few layers of the as-EBM Ti-6Al-4V sample was characterised as α′ plates [15]. This was attributed to the rapid cooling rate higher than 410°C/s for the EBM process which is the critical cooling rate to trigger martensite formation [15]. When an EBM Ti-6Al-4V sample with a wall thickness of < 1 mm was fabricated, a mixed microstructure of α+β and α′ plates was observed [15], suggesting that the microstructure of this alloy is very sensitive to the cooling condition [15,16].

Several research groups for example in [10,17] have reported the presence of graded microstructures in the as-EBM Ti-6Al-4V along the build direction (along the vertical Z-axis). Murr et al. [17] found that the average α lath width within columnar prior β grains varied from 1.6 μm at the bottom (Z=10 mm, where Z=0 is the bottom of the sample) to 3.2 μm at the top of the build (Z=58 mm). Similarly, Tan et al. [10] found an increased α lath width from 0.58±0.11 μm at the bottom (Z=4 mm) to 0.77 ± 0.20 μm at the top (Z=24 mm). In the same work, columnar prior β grain width was found to increase along the build direction from 42.77±14.52 μm (Z=4 mm) to 56.82±13.73 μm (Z=24 mm). Both groups [10,17] also reported that there was a decrease in micro-hardness from the bottom to the top of the EBM build. For instance, Tan et al. [10] correlated the small decrease in micro-hardness from 327 HV1 to 319 HV1 to the α lath width increase from 0.58±0.11 μm to 0.77±0.20 μm, based on the classic Hall-Petch relation. Apart from such a small hardness difference, it is also worthwhile to note in the work by Tan et al. [10] that the micro-hardness of 327 HV1 combined with the presence of fine Widmanstätten microstructure in the as-EBM condition is surprisingly low compared with that of 348 HV1 for wrought Ti-6Al-4V with a larger sized microstructure [2]. Ladani [18] also reported a similar trend in decrease in micro-hardness from 571 HV30 (5.6 GPa) at the bottom to 409 HV30 (4.11 GPa) at the top in 100 mm tall samples. Lu et al. [19] reported a decrease in α lath width from 1.06±0.05 μm at the top (Z=290 mm) to 0.74±0.06 μm at the bottom (Z= 11 mm) in 300 mm long rods. The yield strength increased from 903.6±24.6 MPa at the top to 911.9±34.3 MPa at the bottom of the rod in the as-built state. But, no correlation was reported between the microstructure parameter (i.e. α lath width) and the mechanical property (i.e. yield strength). In contrast, Hrabe et al. [20] did not find any gradient in both the α lath width and mechanical properties along the build direction in as-EBM Ti-6Al-4V with a total build height of 27 mm. The columnar prior β grain width changes from the bottom to the top was also not reported in as-EBM Ti-6Al-4V samples in [18].

To provide an unambiguous assessment of the presence of graded microstructure and associated mechanical property variation along the build direction of EBM-built Ti-6Al-4V, it is essential to consider a tall EBM sample block. To this end, two EBM sample blocks were fabricated with a total build height of 380 mm and 120 mm respectively. The present paper reports a critical evaluation of the

microstructural gradient from the bottom to the top of these two sample sets. Micro-hardness measurements were performed to provide a comparison with the literature data and used as an indication of the material yield strength. The results were analysed and are presented using the size-distribution histogram with log-normal fitting as well as the box and whisker diagram to allow us to draw conclusions on the statistical distribution of the data. A comprehensive understanding of the resulting microstructural gradient as well as the variation in mechanical properties is of particularly importance to aerospace industry where large-scale safety-critical engineering parts are already EBM fabricated; for example the EBM-built front bearing for a Trent XWB-97 engine [21].

2. Experimental

2.1 Materials fabrication

Two EBM Ti-6Al-4V sample sets were prepared: round bars (380 mm build height) and rectangular plates (120 mm build height). We use RB and RP throughout the present paper as abbreviations for Round Bar and Rectangular Plate respectively. Dimensions of both sample sets and their layouts are shown in Fig. 1a and 2a. The EBM build direction is designated as Z-axis. A batch of four RB samples each with diameter of 14 mm and build height of 380 mm were fabricated using an Arcam A2XX system with control software version 3.2, as shown in Fig. 1a. A standard Arcam build theme for Ti-6Al-4V (Arcam AB, Mölndal, Sweden) was used with a layer thickness of 70 μm and an accelerating voltage 60 kV. The entire EBM process was carried out under a vacuum pressure of ~2 × 10^{-3} mbar, controlled by using high-purity helium as a regulating gas to prevent powder charging. A batch of six RP samples with each width of 100 mm, thickness of 15 mm and build height of 120 mm were produced using an Arcam Q20plus system with control software version 5.0, Fig. 2a. Similarly, a standard Arcam build theme for Ti-6Al-4V (Arcam AB, Mölndal, Sweden) was used with a layer thickness of 90 μm and accelerating voltage 60 kV. The entire process was carried out under a vacuum pressure of ~4 × 10^{-3} mbar.
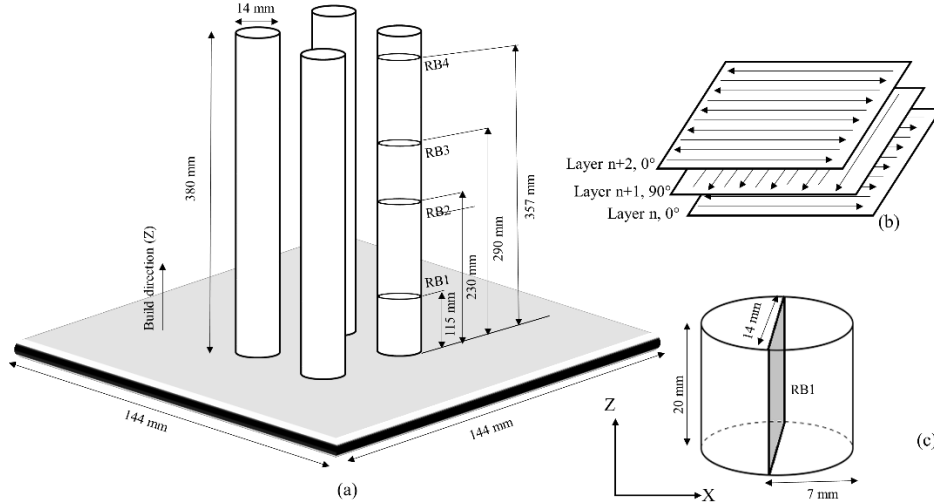
Fig. 1. Schematic representation of (a) dimensions of EBM built Ti-6Al-4V round bar, (b) scanning strategy used to build the round bar (the hatching direction is changed by 90° after each build layer), (c) the relative sample position used for microstructural evaluations

A 10 mm thick stainless steel start plate with a surface area of 300×220 mm^2 and a pre-heat area of 144×144 mm^2 was used for RB sample build, while the pre-heat area for RP sample builds was 190×190 mm^2. As shown in Fig.1a and 2a, the RB and RP samples were positioned close to centre position of the start plate. The plate was pre-heated by electron beam to a build temperature of ~720°C, that was measured by a thermocouple[1] connected to the bottom of the plate. No supports were applied for the EBM fabrication. The Ti-6Al-4V powders were raked onto the plate prior to pre-heating. This was followed by contour melting and hatch melting. This procedure was repeated layer-by-layer. The total fabrication time was 91 h[2] for RB samples and 28 h for RP samples. The samples were cooled within the EBM chamber to room temperature in approximately 5 h for RB samples and 2 h for RP samples.

---

[1] Note: the thermocouple was not used as a closed loop control system to modify the pre-defined EBM processing parameters. This is a common practice for any Arcam EBM machines.

[2] Apart from the four RB samples, a Ti-6Al-4V part was built in the same batch. This accounts for the relatively long total fabrication time. The exact sample part cannot be indicated here due to industrial confidentiality.
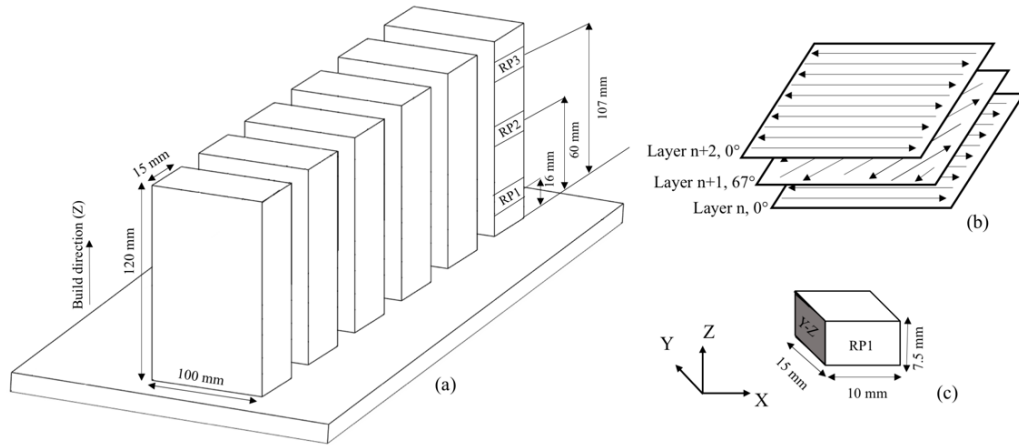
Fig. 2. Schematic representation of (a) dimensions of EBM built Ti-6Al-4V rectangular plate, (b) scanning strategy used to build the round bar (the hatching direction is changed by 67° after each build layer), (c) the relative sample position used for microstructural evaluations

A specific hatch melting process parameter combination of beam current, line offset and scanning speed is known to play a vital role in determining the resulting microstructures. Numerical simulation together with experimental validation to interpret the reasons behind have been presented elsewhere [21,22], hence this section primarily focuses on some important differences between the two EBM hatch melting control software version 3.2 and 5.0 used for RB and RP samples respectively. As mentioned earlier, both sample sets were built using a standard Arcam build strategy which is commonly used in industry to EBM fabricate large-scale engineering parts with the complex geometry. The speed factor, an Arcam pre-defined parameter, describes the functional relationship between the beam current and scanning speed that is appropriate for a given material and melt pool size. An increased speed factor means a reduced energy input and hence leads to a decrease in the melt pool size [20]. A too low speed factor may give high evaporation of light alloy elements (e.g. Al for Ti-6Al-4V) while a too high speed factor may result in incomplete fusion between layers (e.g. lack-of-fusion defects). The Q20plus system had higher beam sharpness as compared to A2XX which is evident from the lower beam radius (0.15-0.20 mm) for Q20plus in contrast with A2XX (beam radius 0.25-0.30mm). The line offset that describes the offset between each scanning line was 0.20 mm for RB samples and 0.22 for RP samples. The key EBM hatch melting parameters are summarised in Table 1.

Table 1. EBM processing parameters used for round bars (RB) with a total build height of 380 mm and rectangular plates (RP) with a total build height of 120 mm

Sample ID	Speed factor	Line offset (mm)	Beam current (mA)	Beam radius (mm)	EBM Arcam platform
RB	36	0.20	17	0.25-0.30	A2XX
RP	33	0.22	19	0.15-0.20	Q20plus

For the EBM control software version 3.2 (used for RB samples), the beam current is scan length dependent (beam current and scanning speed are adjusted with part geometry) and either 0° or 90° hatch direction is used for each layer, whereas the beam current is scan length independent (a constant solidification rate and thermal gradient) and both the global and regional hatch rotation are applied for software version 5.0 (used for RP samples). Fig. 1b shows the hatch melting strategy used for the RB samples, where the hatch direction was changed by 90° after each build layer. Fig. 2b shows the hatch melting strategy used for the RP samples, where the hatch direction was changed by 67°.

Arcam plasma atomised Ti-6Al-4V (Grade 5) powder with particle size ranging between 45-106 µm was used for the RB samples (380 mm build height), whereas Arcam gas atomised Ti-6Al-4V (Grade 5) powder with the same particle size range was used for the RP samples (120 mm build height). Gas atomised powders are mostly spherical but tend to have some asymmetric particles and satellites while plasma atomisation can produce highly spherical particles. Also, compared to gas atomisation, plasma atomisation can provide more consistent results in terms of producing powders and this gives improved mechanical properties in the final part due to removal of excess oxygen from the powder [24]. The inert gas fusion method (ASTM E1409) was used to measure the H, O and N contents and plasma spectroscopy (ASTM E2371) was used to measure the other key elements for RB virgin Ti-6Al-4V powders as well as for RP reused Ti-6Al-4V powders. The chemical compositions of both Ti-6Al-4V powders presented in Table 2 which are consistent with the nominal chemical compositions for Arcam Ti-6Al-4V powders [25,26]. The compositions of as-built Ti-6Al-4V RB and RP samples are also listed in Table 2. The Al content decreased from 6.46 to 5.43 wt% for RB sample and from 6.52 to 5.65 wt% for RP sample. This decrease can be due to the evaporation of Al at high temperature (~720°C) of EBM process. The similar decrease was also reported in the

work of Lu et al. [19]. The oxygen content in the as-built Ti-6Al-4V RB sample was found to increase from 0.17 to 0.20 wt% . The similar increase was also reported in the work of Lu et al. [19]. This can be due to oxygen pick up during high temperature (~720°C) EBM process. The oxygen content in the as-built Ti-6Al-4V RP sample was found to decrease from 0.19 to 0.12 wt%.

Table 2. Chemical compositions (wt%) of Ti-6Al-4V powders

Sample ID	Al	Fe	N	O	Sn	V	Balance
Virgin plasma atomised powders (RB samples)	6.46	0.16	0.027	0.17	0.01	4.14	Ti
Reused gas atomised powders (RP samples)	6.52	0.17	0.029	0.19	-	4.12	Ti
As-built RB	5.43	0.17	0.030	0.20	-	4.35	Ti
As-built RP	5.65	0.18	0.029	0.12*	-	4.39	Ti

* It is very unlikely that the oxygen content decreases in the as-built sample. The decrease in the oxygen content might be due to a bubble being created at the end in the crucible while analysis and gases being trapped there.

2.2 Metallography

Four samples were extracted from one of the four identical RB samples, as indicated in Fig. 1a, along the build direction at different Z heights of Z=115, 230, 290 and 357 mm. These four metallographic samples are named as RB1 (Z=115 mm), RB2 (Z=230 mm), RB3 (Z=290 mm) and RB4 (Z=357 mm) from bottom to top of the EBM build. Sample RB1, RB2 and RB4 were each 20 mm high, as shown in Fig. 1c, while RB3 was 10 mm high. Three metallographic samples each having a dimension of 10 mm × 15 mm × 7.5 mm as illustrated in Fig. 2c were extracted from one of the six identical RP samples along the build direction at different Z heights of Z=16, 60, and 107 mm. These three samples are named as RP1 (Z=16 mm), RP2 (Z=60 mm) and RP3 (Z=107 mm) respectively, see Fig. 2a. Both the microstructural and micro-hardness characterisations were performed on the longitudinal cross-section plane for all samples to evaluate the change in prior β grain width, α lath width and mechanical property along the EBM build direction. All metallography examinations were

performed at centre position of the EBM-built sample, away from the contour melting areas.

Samples were prepared using standard metallographic procedures including mounting, grinding with SiC papers down to a grit size of 2500 and polishing using diamond suspension down to 1 μm, followed by the final OPS polishing with colloidal silica of 0.02 μm particle size. To reveal microstructural features, the polished samples were etched with Kroll's reagent (96 ml H_2O, 2 ml HF, and 6 ml HNO_3) for ~45 seconds. Columnar prior β grain width measurements were carried out using ImageJ [27] on low magnification images taken by using an optical microscope (Zeiss LSM 780). For each sample, more than 200 individual measurements were made. Multiple readings per prior β grain were taken and then averaged. Sometimes, there is not always grain boundary α to help distinguish prior β grain boundaries. Hence, the measurements were performed only on clearer prior β grains boundaries. Similar approach was also adopted in the previous work [28]. A Zeiss Gemini Sigma 500VP scanning electron microscope (SEM) with an operating voltage of 10 kV was used for detailed microstructural analysis. The α lath width measurements were carried out on all samples (RB1 to RB4 and RP1 to RP3) using high magnification SEM images. In practice, the α lath width was determined by measuring the distance between two neighbouring β rods which is a bright phase shown in Fig. 7. This measurement method was also adopted in previous work [10,19]. For each sample, approximately 300 individual measurements were performed using ImageJ. Furthermore, the presence of porosity and/or lack-of-fusion defects was assessed by using the SEM equipped with energy dispersive X-ray spectroscopy (EDS, Oxford Instruments) at 20 kV. The size of pores was measured by using ImageJ on high magnification SEM images. The images were cropped and reduced to 8-bit colour using the ImageJ software. After taking automatic threshold, the "Analyse Particles" function was utilised to retrieve the pore data and porosity in terms of area fraction.

2.3 Micro-hardness

Samples prepared for microstructural examination were also subjected to Vickers micro-hardness measurements using D80 Durascan-70 by EmcoTest under 0.5 kgf load (HV0.5) for 10 seconds to investigate the likely effect of the graded microstructures on material yield strength along the build direction. These samples

included RB1 (Z=115 mm), RB2 (Z=230 mm), RB3 (Z=290 mm) and RB4 (Z=357 mm) as well as RP1 (Z=16 mm), RP2 (Z=60 mm) and RP3 (Z=107 mm). At least 40 measurement points were performed for each sample.

2.4 Statistical data analysis

It was noticed that the repeatability of the α lath width measurement was not high. This was mainly due to the complex α+β microstructure with both Widmanstätten and colony morphology in as-EBM Ti-6Al-4V. The presence of prior β-phase in a mixed discrete rods and dots morphology made the measurements even more difficult. To overcome this barrier, a statistical approach was taken to present the measurement data using the size-distribution histogram, as illustrated in Fig. 8a and 8b. This allows an unambiguous comparison of the different microstructures along the EBM build direction. Furthermore, the α lath width size-distribution histograms, as illustrated in Fig. 8a and 8b, showed an asymmetry of the probability distribution with a noticeable positive skewness. As a result, a log-normal distribution curve, instead of the more commonly-used normal distribution, was used to fit the size-distribution histogram data. This applies to all samples including RB1 to RB4 and RP1 to RP3. Detailed information about the size-distribution and derived statistically significant values will be given in in Section 3.2.

The columnar prior β grain width for each sample is presented by using size-distribution histograms with size intervals of 20 μm, similar to those adopted for the α lath width but with size intervals of 0.2 μm. In addition, the micro-hardness data collected along the EBM build direction at different build height positions are presented using the box and whisker diagram to graphically compare hardness data through their percentiles in addition to mean values, as illustrated in Fig. 9. The horizontal line in each rectangular block represents the mean value, the ends of the box are the 25th percentile (lower end) and 75th percentile (upper end) and the spans show the highest and lowest hardness values obtained for the sample. This offers evidence of a statistically significant difference in terms of the measured mechanical property gradient along the EBM build direction.

3. Results

3.1 Ti-6Al-4V powders

The secondary electron SEM images of Ti-6Al-4V powders and the particle size distribution are presented in Fig. 3. The characterisation was done on the reused gas atomised powders. The powder particles with different sizes (27-163 µm) are distributed homogeneously. The powder particles are mostly spherical but some irregular-shaped particles (satellite particles) can also be seen in Fig. 3a and 3b. The particles have a martensitic needle-like microstructure (Fig. 3c) as a result of rapid cooling during atomisation. This is consistent with the work of Qiu et al. [29]. Pores are also present in some of the powder particles possibly due to gas entrapment (Fig. 3b and 3c). The powder particle size distribution analysis is presented in Fig. 3d. It can be seen that 90% of the powder particles fall into the size range of 45 and 106 µm. The mean diameter of the particles was found to be 78 µm. The figure also shows a small fraction of particles with sizes smaller than 10 µm which corresponds to the satellite particles as seen in Fig. 3b.
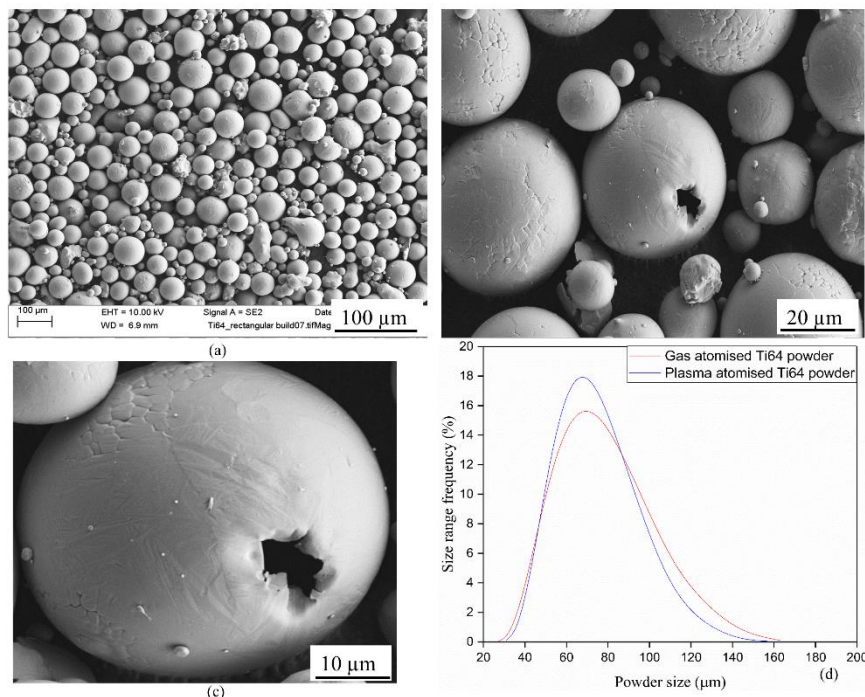

Fig. 3. SEM images showing (a) most of the powders are spherical; (b) and (c) martensitic needle structure at the powder surface and a pore possibly due to gas entrapment; and (d) powder particle size distribution

3.2 Graded microstructure

Fig. 4a and 4b show optical micrographs of the columnar prior β grains in sample RB1 (Z=115 mm) and RB4 (Z= 357 mm) respectively. The Z-direction runs from the bottom to the top for each image. The columnar prior β grains oriented along the Z-direction with a continuous α-phase along grain boundaries. As the α-phase is etched out by Kroll's reagent, it exhibits bright contrast and prior β-phase exhibits dark contrast under the optical microscope. Such a columnar prior β grain microstructure was observed for most as-EBM Ti-6Al-4V [13,14]. Fig. 4c and 4d show optical micrographs for sample RP1 (Z=16 mm) and RP3 (Z=107 mm) respectively. The observed columnar prior β grains in RP samples, Fig. 4c and 4d, is similar to those in RB samples, Fig. 4a and 4b.
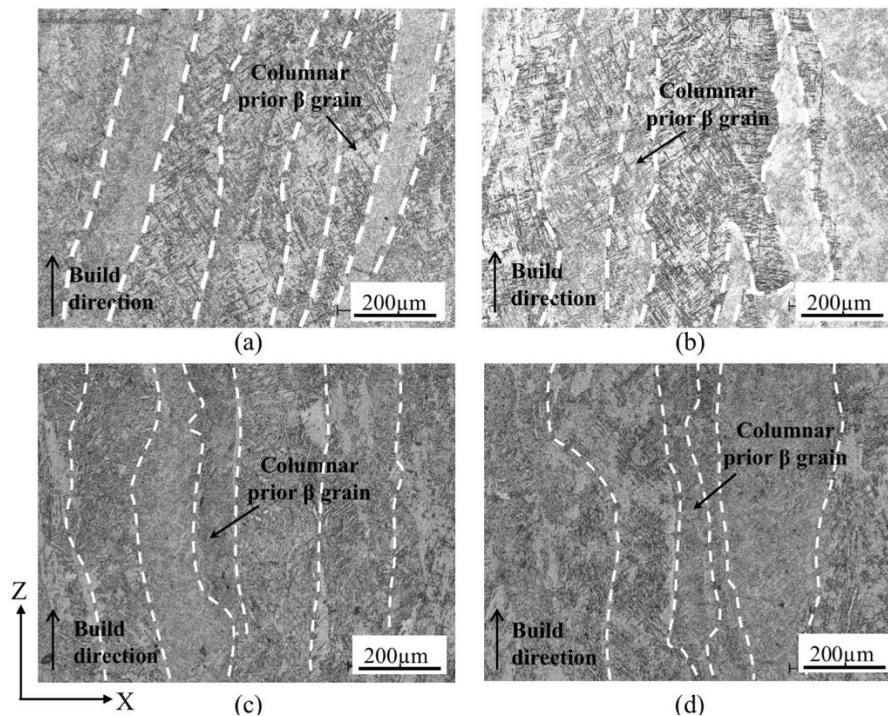

Fig. 4. Optical micrographs showing columnar prior β grains oriented along the build direction in (a) round bars at Z=115 mm (RB1), (b) Z=357 mm (RB4), and (c) rectangular plate builds at Z=16 mm (RP1) and (d) Z=107 mm (RP3). Dark and bright areas show β and α phase respectively.

The prior β grain width size-distribution histograms for RB and RP samples are presented in Fig. 5 and Fig. 6 respectively. The mean prior β grain width gradually increased with the build height from 86±38 µm in RB1 (Z=115 mm, Fig 5a) to

13

154±56 µm in RB4 (Z=357 mm, Fig. 5d) for RB samples with a total build height of 380 mm. For the RP samples, a similar increase in the prior β grain width along the build direction can also be seen, where RP1 (Z=16 mm, Fig. 6a) had a mean prior β grain width of 79±34 µm and RP3 (Z=107 mm, Fig. 6c) had a value of 122±56 µm. Therefore, it is clear that samples extracted from the bottom of the EBM build had the smallest prior β grain width, whereas the top samples had the largest grain width.
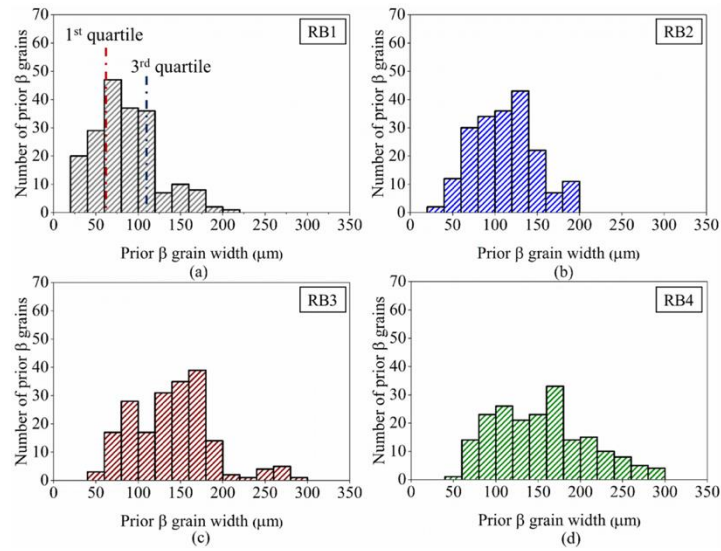

Fig. 5. Prior β grain width size-distribution histograms for round bar samples, (a) RB1 (Z=115 mm), (b) RB2 (Z=230 mm), (c) RB3 (Z=290 mm) and (d) RB4 (Z=357 mm)
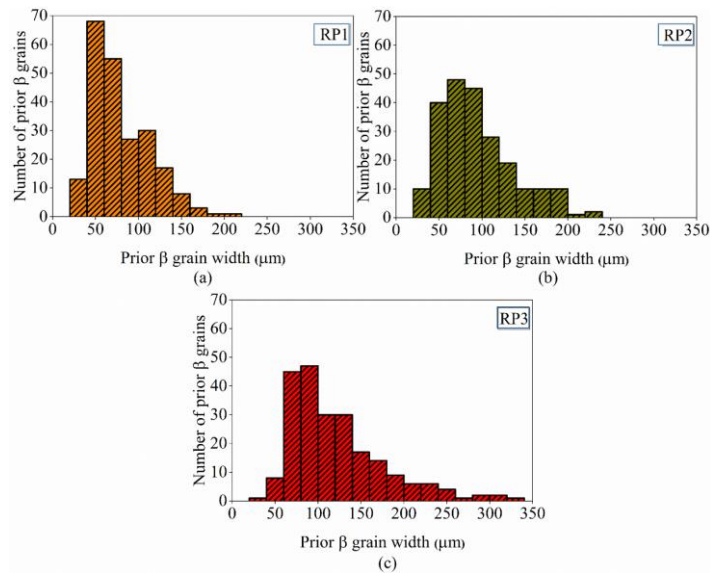

Fig. 6. Prior β grain width size-distribution histograms for rectangular plate, (a) RP1 (Z=16 mm), (b) RP2 (Z=60 mm) and (c) RB3 (Z=107 mm)

The 1ˢᵗ quartile (25ᵗʰ percentile) and 3ʳᵈ quartile (75ᵗʰ percentile), as indicated in Fig. 5a, of prior β grain width were determined to be 61 µm and 109 µm in RB1 (Z=115 mm, Fig. 5a), 83 µm and 137 µm in RB2 (Z=230 mm, Fig. 5b), 104 µm and 167 µm in RB3 (Z=290 mm, Fig. 5c), and 109 µm and 185 µm in RB4 (Z=357 mm, Fig. 5d). Similarly, for RP samples, the 1ˢᵗ and 3ʳᵈ quartile prior β grain width were measured to be 52 µm and 102 µm in RP1 (Z=16 mm, Fig. 6a), 63 µm and 116 µm in RP2 (Z=60 mm, Fig. 6b) and 81 µm and 145 µm in RP3 (Z=107 mm, Fig. 6c). These statistical values further evidence that the prior β grain width increased along the EBM build height. A closer look at the size-distribution histograms, Fig. 5a to 5d and Fig. 6a to 6c, reveals that the number of smaller prior β grains decreased with the increase in EBM build height, confirming a graded prior β grain width along the build direction. The samples at a higher build height, RB4 and RP3 had a higher number of prior β grains with the grain width of greater than 200 µm, Fig. 5d and Fig. 6c, as compared to RB1 and RP1, Fig. 5a and Fig. 6a. Furthermore, samples extracted from the RB build processed using the A2XX EBM machine show a fewer number of smaller sized prior β grains (< 100 µm in grain width) compared to the RP build processed using the Q20plus EBM machine. Table 3 summarises the mean value and standard deviation STDEV for the prior β grain width; these are most often used when the measured values are presented in literature. It can be seen in Table 3 that the mean prior β grain width comes with a large STDEV. This deviation is a result of large size-distribution for the measured columnar β grains, as evidenced in the size-distribution histograms in Fig. 5 and Fig. 6.

The α+β microstructure typically observed in the RB and the RP samples are shown in Fig. 7a and 7b respectively. Within the prior β grain, the α+β microstructure with both Widmanstätten and colony morphology can be observed. α laths are oriented in various directions. The prior β-phase (a brighter colour) is shown as rod and dot-like morphology embedded within the α-phase (a darker colour), similar to the observations reported in [10]. Fig. 7c and 7d show two distinct microstructures that are formed at either side of a grain boundary α-phase; Widmanstätten and colony morphology (marked by red dotted outline).
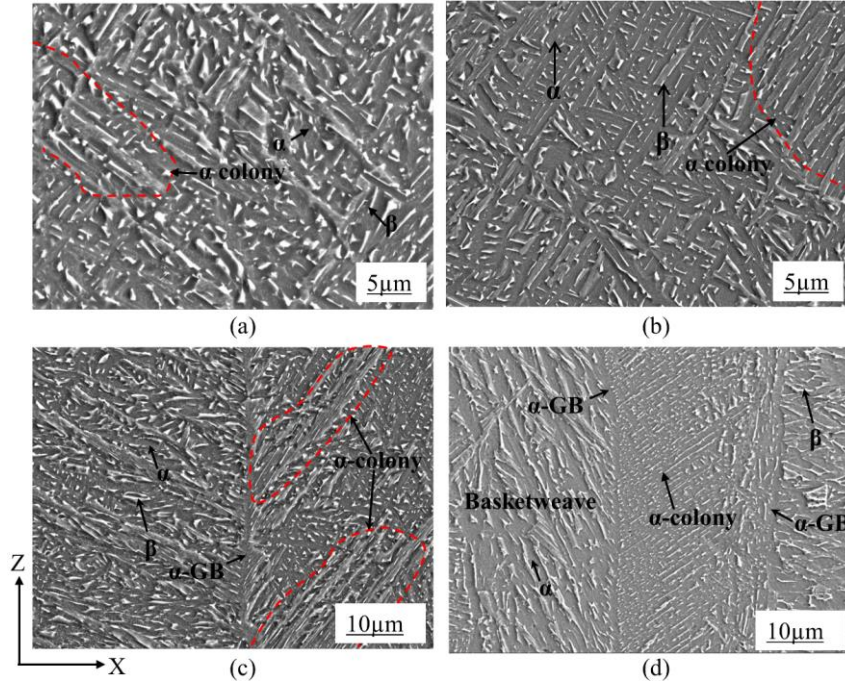
Fig. 7. SEM images showing α+β microstructure consists of both Widmanstätten and colony morphology in (a) round bar and (b) rectangular plate samples. Formation of α+β both in Widmanstätten and colony morphology along one α-GB in (c) round bar (d) rectangular plate builds (dark and bright areas show α and β phase respectively)

Table 3. Summary of prior β grain width, α lath width and micro-hardness measurements in round bar and rectangular plate builds

Sample ID	β grain width (µm)	α lath width			Hardness (HV0.5)
		Mean (µm)	Median (µm)	Mode (µm)	
RB1 (Z=115 mm)	86±38	0.58±0.24	0.55	0.46	406±12
RB2 (Z=230 mm)	112±37	0.61±0.26	0.56	0.47	390±6
RB3 (Z=290 mm)	139±47	0.68±0.30	0.63	0.51	386±12
RB4 (Z=357 mm)	154±56	0.87±0.33	0.81	0.69	382±16
RP1 (Z=16 mm)	79±34	0.96±0.45	0.93	0.63	342±9
RP2 (Z=60 mm)	94±43	1.02±0.43	0.94	0.78	336±8
RP3 (Z=107 mm)	122±56	1.10±0.49	1.02	0.85	329±15

The α lath width size-distribution histograms for RB and RP samples are presented in Fig. 8a and 8b respectively. The α lath width varied from 0.19 µm in RB1 to 2.17 µm in RB4 for the round bar build, Fig. 8a. A similar size variation from

0.17 µm in RP1 to 3.20 µm in RP3 for the rectangular plate build can be seen in Fig. 8b. Both the RB and RP builds show the trend of a decrease in the number of smaller α laths with the increase in build height indicating the graded microstructure in as-EBM Ti-6Al-4V. In addition, at any given location along the build height, the number of smaller α laths are higher for the RB samples compared to the RP samples. This resulted in the mean α lath width (see Table 3) for the former to be smaller compared to the latter. For both the EBM builds, the mean α lath width gradually increased with the build height. Samples extracted from the bottom of the EBM build show the least mean α lath width (0.58±0.24 µm in RB1 and 0.96±0.45 µm in RP1, Table 3) and the samples extracted from the top show the highest mean α lath width (0.87±0.33 µm in RB4 and 1.10±0.49 µm in RP3, Table 3).
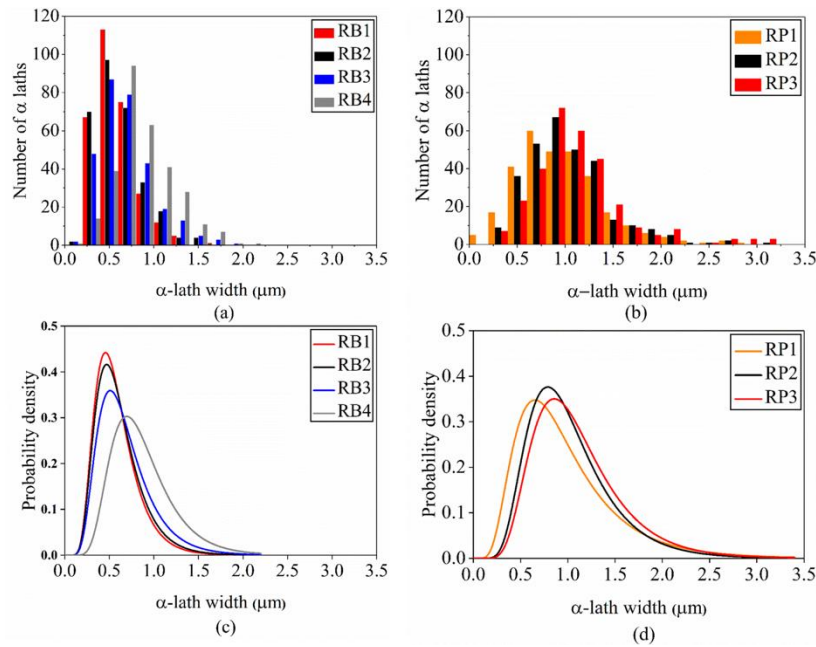

Fig. 8. α lath width distribution histogram for (a) round bar (b) rectangular plate build and the log-normal size-distribution plots for (c) round bar (d) rectangular plate build

The log-normal plots based on the size-distribution histograms of the α lath width, Fig. 8c and Fig. 8d, are used to provide a statistical interpretation of the measured data. Both figures clearly show the presence of a positive skewness in the α lath width distribution. The mode and median values of the α lath width are also presented in Table 3. The mode is α lath width value corresponding to the highest probability density shown in Fig. 8c and 8d, while the median is the midpoint separating the lower and upper halves of the measured α lath width values. Note that the mean and median values of α lath width population are well represented by the

respective values from RB and RP samples, but the mode values are heavily influenced by the counting statistics. In this regard, the peaks of the fitted log-normal distributions in Fig. 8c and 8d is treated as representative of the most likely population value. For both the builds, the distribution curve is shifted to the right confirming that the mean α lath width as well as the median increases with the build height. The increase in median from bottom to top indicates that there is a higher probability of observing a higher α lath width value at a given upper height than that at the lower height with an increase in build height. For the RB build, the probability of the presence of smaller sized α lath width decreases together with an increasing proportion of the larger sized α lath width along the build height, Fig. 8c. This also applies to RP build, Fig. 8d. One of the interesting findings when comparing the RB (A2XX machine) and RP (Q20plus machine) builds is that the skewness observed in the latter is higher for the RP build. In other words, a higher proportion of larger sized α lath width was created in as-EBM Ti-6Al-4V alloy processed by using Q20plus machine with the standard Arcam build theme.

3.3 Micro-hardness gradient

To determine the graded hardness along the build height, micro-hardness measurements were carried out both the EBM builds. The mean Vickers micro-hardness HV0.5 are presented in Table 3. Overall, the mean hardness decreases with the build height from 406±12 in RB1 to 382±16 in RB4, and from 341±11 in RP1 to 328±15 in RP3. These values are in good agreement with the observed graded microstructure along the EBM build. Furthermore, the mean micro-hardness for the RB build is higher than the RP build, which again is consistent with the smaller sized α lath width observed in the RB build.

It is worth noting that there is a noticeable variation in hardness measurements for all the specimens. The hardness variation at a given location along the EBM build is presented as box and whisker plots in Fig. 9. The mean hardness shows a decreasing trend with the increase in build height, although the presence of variation in the measured hardness. The horizontal line in the middle of a box represents the mean value (data are given in Table 3). The horizontal lines at the lower and upper

end of a box are the 25th and 75th percentiles respectively. A percentile is the number where a certain percentage of values fall below that number.
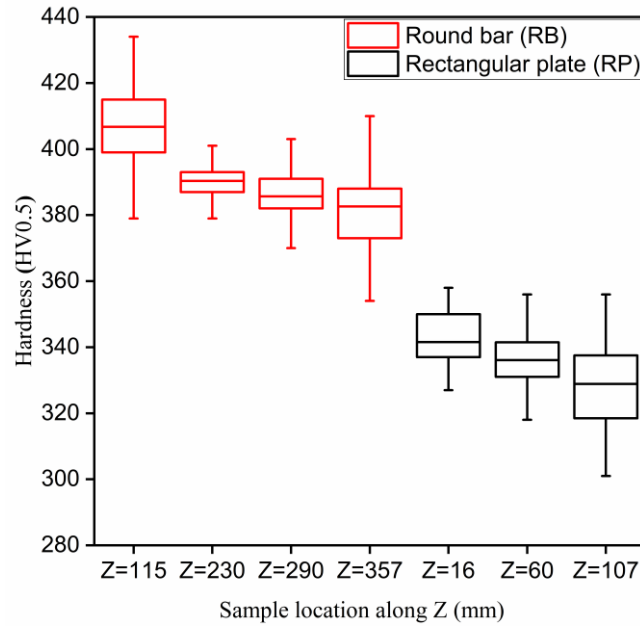

Fig. 9. Box and whisker plot showing mean hardness and hardness variation in X-Z plane in round bar RB and rectangular plate RP builds

3.4 Microstructural analysis of the top few layers

Some studies [15,16] have reported the presence of martensitic α′ plates at the top few layers of an as-EBM Ti-6Al-4V. Such martensitic α′ plates gradually decomposed to fully dense acicular α lath due to long exposures at high build temperature [13]. The top 0.65 mm regions for both the RB and RP builds were examined. The presence of α′ martensitic microstructure was found and they were only limited to the top few layers, Fig. 10a and 10b respectively. The layers just below the top 0.65 mm region exhibit the formation of α+β microstructure with both Widmanstätten and colony morphology as shown in Fig. 10c and 10d. The presence of α′ martensitic microstructure would lead to a micro-hardness elevation close to the EBM build top surface. The micro-hardness of the martensitic phase was found to be 383 HV0.1 for the RP build and 390 HV0.1 for the RB build. The micro-hardness decreases as a function of the distance away from the top layers as presented in Fig. 11b and the corresponding optical micrograph at a low magnification is shown in Fig. 11a. The presence of a distinct layer boundary at around the top 0.65 mm can be seen in Fig. 11a.
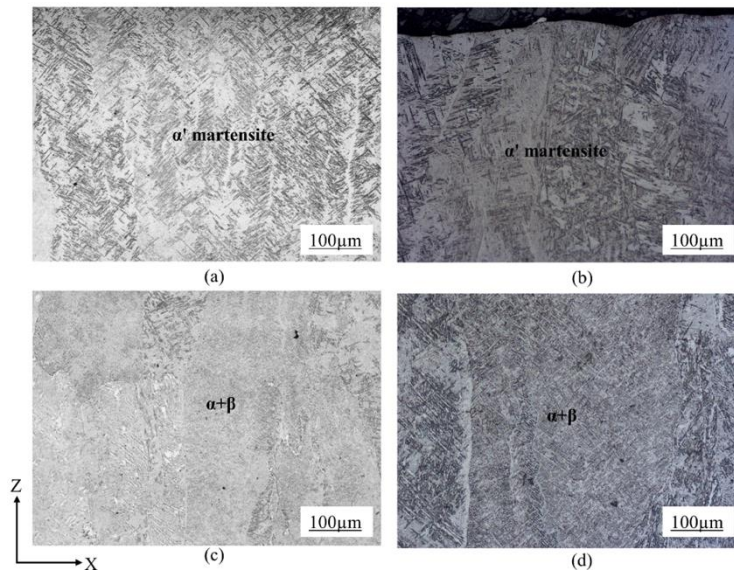
Fig. 10. Optical micrographs: (a) round bar and (b) rectangular plate build in the top 0.65 mm regions showing the presence of α′ martensite, and (c) round bar and (d) rectangular plate in the regions of just below the top 0.65 mm region showing the presence of α+β microstructure.
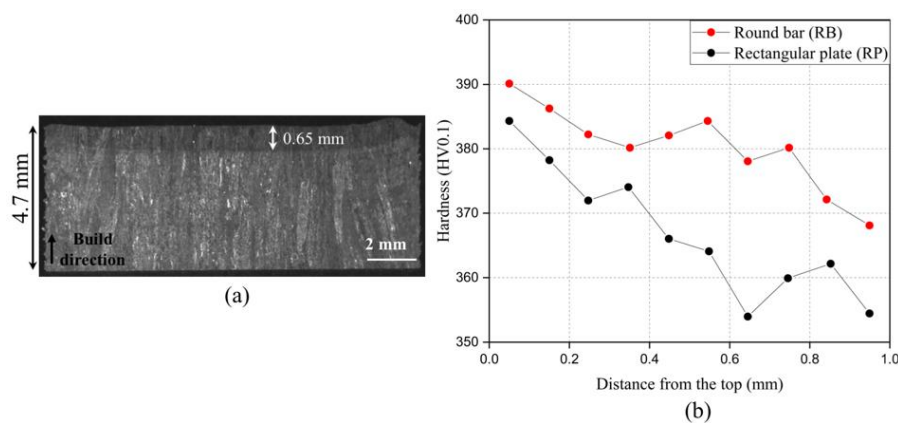
Fig. 11. (a) A low magnification optical micrograph showing the micro-hardness measurement position at the top layer, (b) Changes in micro-hardness with the distance moving away from the top layer.

3.5 Porosity analysis

Two types of defects were found in the two EBM builds; spherical gas pores (see Fig. 12a and 12d) and irregularly shaped lack-of-fusion defects (see Fig. 12c and 12f). The observed gas pores are near spherical with mean diameters of 41±23 µm and 35±16 µm in RB and RP samples respectively. In addition, gas pores filled with partially melt powders were also found for both the RB and RP samples, see Fig. 12b

and 12e. The EDS analysis performed on these gas pores showed that the partially melted powders contain a higher concentration of titanium (see Table 4). This applies to both the RB and RP samples. The EDS analysis locations are highlighted in Fig. 12b and 12e. It was confirmed that there was no gradient along the build direction in terms of the area fraction of the pores (0.07%) and lack-of-fusion defects. The area fraction of the pores and lack-of-fusion defects was very low (less than 0.1%), so that it is not expected that these defects would have any significant effect on the strength of EBM built samples with taller builds. This is consistent with the work of He et al. [30]. Furthermore, an essentially defect free material is possible to obtain after Hot Isostatic Pressing (HIP) as is shown in the work of Lu et al. [19] where the density of EBM built Ti-6Al-4V was found to increase from 99.03% in as-built condition to 99.90% after HIP.
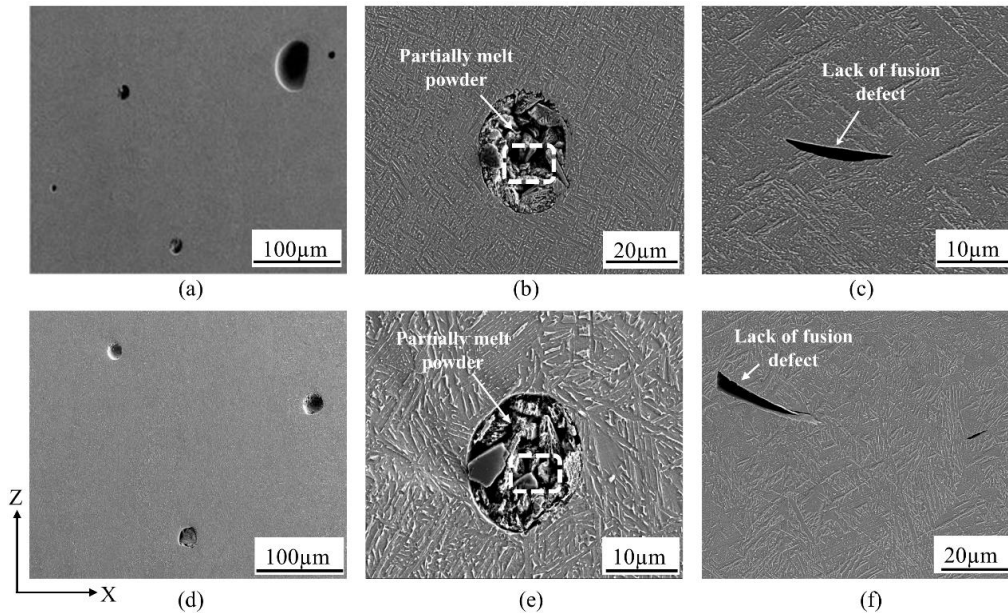
Fig. 12. SEM images of EBM Ti-6Al-4V showing (a) to (c) gas pore, gas pore filled with partially melted Ti-6Al-4V powder and a lack-of-fusion defect in RB samples, (d) to (e) gas pore, gas pore filled with partially melted Ti-6Al-4V powder, lack-of-fusion defect in RP samples.

Table 4. Chemical composition of gas pores filled with partially melt powder using EDS (wt%)

Sample ID	Ti	Al	Fe	O	Sn	V
RB	62.80	4.60	0.30	19.70	0.01	2.60
RP	73.00	3.60	0.26	14.05	-	3.46

4. Discussion

The α lath width in as-EBM Ti-6Al-4V depends on the cooling rate of the material in the whole sample. In other words, it is determined by the scanning strategy, build height and sample geometry. The impact of all of these factors is assessed in the following sections. The linkage of the mean, median and modal α lath width values to the variation in hardness is also discussed.

4.1 EBM processing parameters

Two different melting strategies (standard build theme for Ti-6Al-4V control software version 3.2 and 5.0) were used for processing round bar RB samples, Fig. 1b, and rectangular plate RP samples, Fig. 2b. This results in similar Widmanstätten and lamellar α colony microstructures from bottom to the top of the EBM build irrespective of the sample geometry and melting strategy, see Fig. 7. However, the RB samples that were built with Arcam A2XX control software version 3.2 exhibited a finer size of α laths, Fig. 8a, compared to those observed in the RP samples that were built with Arcam Q20plus control software 5.0, Fig. 8b. This can be attributed to the different cooling rates that were experienced by these two different EBM builds. According to Hrabe and Quinn [31] the speed factor has an inverse relationship to the energy input and melt pool size, and the cooling rate decreases with the increase in energy input and melt pool size. In the present study, the higher speed factor of 36 was used for RB samples compared to RP samples where a speed factor of 33 was used, Table 1. In addition, a higher beam current of 19 mA was used for RP samples when compared to that of 17 mA for RB samples. Note the energy input is directly proportional to the beam current. In sum, a combination of the higher speed factor and smaller beam current led to a higher cooling rate and resulting finer α laths in the RB samples as compared to the RP samples. It is evident that the observed size difference in α laths can be correlated with the measured micro-hardness difference, RB samples had a higher micro-hardness than those of RP samples, Fig. 9.

The presence of columnar prior β grains is a direct consequence of directional solidification and large thermal gradients along the EBM build direction. The large thermal gradient is caused by each newly deposited layers where the underlying

solidified layer is also exposed to high temperatures and cycled through the β-transus temperature during the EBM process [10,32,33]. The microstructure evolution in α+β titanium alloys is governed by a complex combination of the cooling rate from high-temperature single β-phase region and the crystallographic orientation of the parent β-phase [34]. EBM built Ti-6Al-4V consists of columnar prior β grains delineated by grain boundary α-phase and a transformed α+β microstructure with both the α colony and Widmanstätten morphology as shown in Fig. 7b and 7c [12]. The α laths start to form at the prior β grain boundaries and grow inward at a certain angle [18]. Fig. 7d shows two adjacent prior β grains exhibited two different microstructures, one being Widmanstätten and the second shows a colony morphology formed along one grain boundary α-phase. The grain boundary α-phase observes the Burgers orientation relationship (12 crystallographic orientations) with only one of the β grain orientations [34]. During the β to α+β phase transformation, the β grain observing the Burgers orientation relationship with a grain boundary α-phase developed a colony microstructure, whereas the adjacent β grain which did not follow the Burgers orientation relationship, instead developed a Widmanstätten microstructure that consisted of most of (if not all) 12 crystallographic variants of α to form a single β grain.

4.2 Effect of cooling rate

The graded microstructure was observed in both the purpose-built RB samples (380 mm total build height) and RP samples (120 mm total build height), the statistical presentation of the measured α lath width across different Z height positions, Fig. 8, show clearly that there is a microstructural gradient running from the bottom to the top of the EBM sample build. An increased proportion of larger sized α laths can be found with the increasing Z height position; this applies to both samples, Fig. 8a and Fig. 8b. There is a temperature gradient during cooling in several different areas, along the build height as well as across the build height of the sample. The interior of the build would be the warmest, and hence the relative temperature would decrease radially outward to the exterior of the build space [31]. The nucleation of α-phase follows an exponential relation with the change in temperature based on Arrhenius equation [35]. The exact solution of Carslaw Jaeger model [36,37] was

found to be applicable to the growth kinetics of α-phase in Ti-6Al-4V; the size of α-phase, R(t), increases with the square root of time, t, if the temperature is held constant, Eq. 1.

$$R(t) = 2q\sqrt{D_i^b t} \qquad (1)$$

where θ denotes the supersaturation that depends on the overall composition and volume fraction of the α-phase and D_i^b is the diffusion coefficient of Al or V in β-phase in Ti-6Al-4V. Quantitative predictions of the volume fraction of α-phase were obtained from an exact solution of Eq. 1 with diffusivities of Al or V adjusted using a standard thermodynamic factor in [34]. The magnitude of diffusion coefficients was found to change exponentially with temperature [37]. Hence, the small variation in temperature due to different cooling rates at different build heights would have a much larger effect on the α lath width size-distribution. The log-normal distribution of α lath width presented in Fig. 8c and 8d in this regard simply maps the big size variation in α lath width due to the small variation in temperature.

It can be observed in Table 3 that both prior β grain width and α lath width increased along the build height. The graded microstructure along the build is the result of different cooling rates, higher and lower cooling rates at the bottom and top of the build respectively. The two major sources of heat loss in an EBM process are through radiation off the top surface and via heat conduction through the sintered powder from the surrounding surface of the specimen and the start plate [10]. Close to the bottom of the build, the heat conduction through the start plate and the substrate resulted in faster cooling rates and subsequent phase transformation resulted in finer α lath width at the bottom of the build compared to the top of the build. As the build process progresses, the thermal conductivity of the Ti-6Al-4V powder bed which is even smaller than the solid Ti-6Al-4V (7 Wm^{-1}K^{-1}) results in lower heat dissipation and higher temperature [19]. As a result, α lath width increased as the build height increased. The heat transfer rate also depends on the sample shape and size, hence, 380 mm tall RB samples due to their much smaller cross-sectional area (14 mm) cool faster and have finer α laths as compared to relatively small 120 mm RP samples, Table 3. According to [32], the thermal gradient in the powder bed is expected to worsen beyond certain powder bed depth causing gradient cooling rate. The graded

microstructure along the build can also be observed from the α lath width distribution results in Fig. 8 that reveals that the number of larger α laths increased with the build height.

4.3 Correlation between microstructure and mechanical property

The graded microstructures resulted in the graded micro-hardness along the build Z-direction, an overall increase in the α lath width from the bottom to the top of the EBM build led to a decrease in micro-hardness, Fig. 9. The relationship between yield strength (or micro-hardness) and a specific material strength-controlling microstructural scale is often presented using the classical Hall-Petch relation (see Eq. 2) for a wide variety of engineering materials [38].

$$H_v = H_0 + k/\sqrt{\lambda}$$
(2)

where H_0 is the intrinsic hardness of the material, k is the Hall-Petch constant, and λ is the microstructural scale in this case the mean α lath width. Fig. 13 presents the Hall-Petch relationship between the measured mean hardness value and the inverse of the square root of the mean α lath width (λ). In general, a good correlation between the change in mean α lath width and micro-hardness was observed for the EBM builds considered in the present work. This can be evidenced by the high value of correlation coefficient, R^2=0.91, for RB and RP samples in terms of the fitted regression lines. The modal and median α lath width values do not show a good correlation with the mean hardness as they failed to show any Hall-Petch type relation. The mean α lath width is thus the best microstructural indicator in terms of controlling the mechanical properties in as-EBM Ti-6Al-4V.
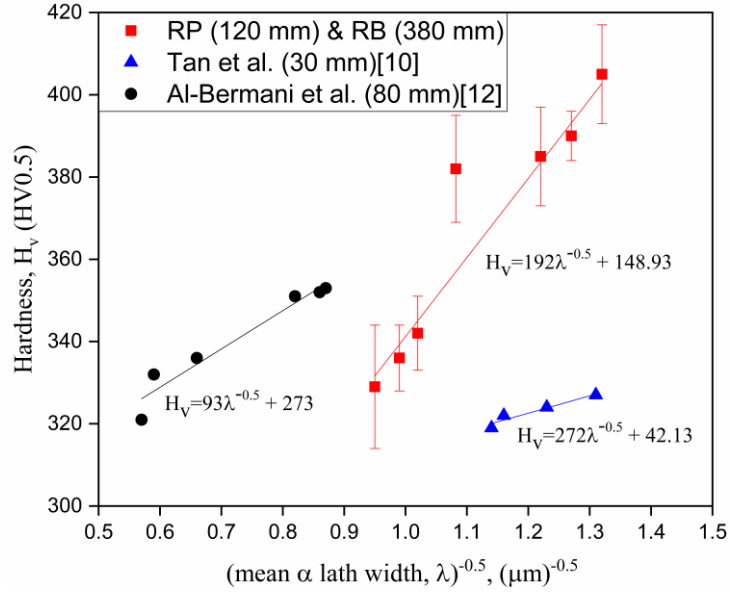
Fig. 13. Variation of mean hardness with inverse of square root of mean α lath width (λ) in RB and RP samples

The variation in the hardness at any given location along the build height, Fig. 13, can be attributed to the change in the local microstructure (α lath width and prior β-phase morphology either in a colony or Widmanstätten type, Fig. 7c and 7d) across each sample. The micro-hardness was higher at the bottom of the build with finer α laths and it decreased with the build height because of the coarser α laths. The Hall-Petch relationship is also consistent with the earlier work [10,12] with much smaller build heights (30 mm and 80 mm respectively) which have been included in Fig. 13 for comparison. Both studies show that the micro-hardness increases with the decreasing microstructural scale (mean α lath width). But in the work by Al-Bermani et al. [12] the effect of build temperature on α lath width and mechanical properties was studied but the gradient in mechanical property due to a change in α lath width along the build height was not reported. This gap is addressed in the present study by showing the strong correlation between hardness and the mean α lath width, Fig. 13. The correlation coefficient of R^2=0.91 obtained in the present work is quite close to that of R^2=0.94 derived from the work of Al-Bermani et al. [12] as shown in Fig. 13. In the work by Tan et al. [10] the increase in hardness was not so high even with significant increase in α lath width. With the increase in α lath width from 0.58±0.11 μm at the bottom (Z=4 mm) to 0.77 ± 0.20 μm at the top (Z=24 mm), the hardness only decreased from 327 HV to 322 HV. Compared to the work of Tan et al. [10] in

terms of the correlation between α lath width and micro-hardness, the present study reveals a strong dependence between mean α lath width and micro-hardness in as-EBM Ti-6Al-4V. In detail, with the small increase in α lath width from 0.97±0.46 μm at the bottom (Z=16 mm) to 1.11 ± 0.49 μm at the top (Z=107 mm), hardness decreased from 341 HV to 328 HV in RP samples as shown in Fig. 9 and Table 3. The large scatter measured in α lath width is likely the cause of some of the confusion in previous studies and only by performing a systematic study over a large build height we can reveal the better understanding of the impact of α lath width on the micro-hardness gradient. It is interesting that the Hall-Petch relationship holds not just in individual data sets of RB and RP samples but across both of the two sample sets as shown in Fig. 13. This suggests that the hardness and therefore static strength of as-EBM Ti-6Al-4V within a single sample is well accounted for by the variation in α lath widths.
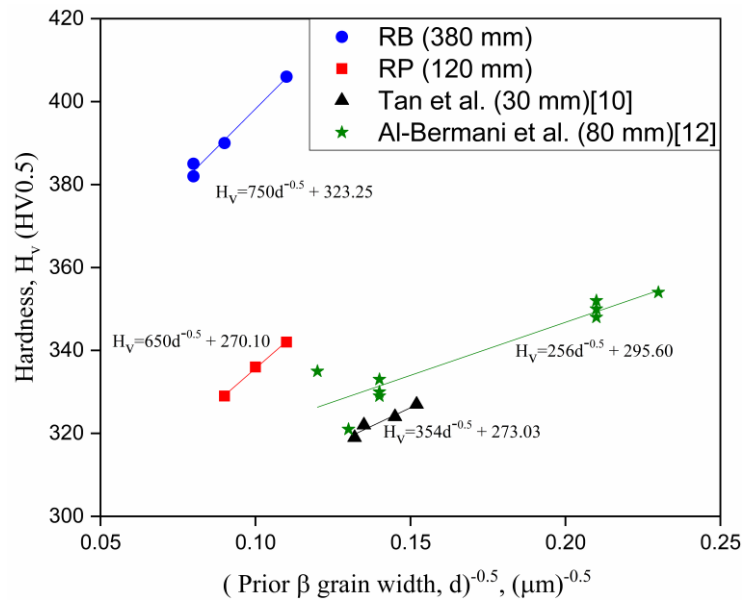

Fig. 14. Variation of mean hardness with inverse of square root of mean prior β grain width (d) in RB and RP samples

The dependence of hardness on mean prior β grain width in RB and RP samples is presented in Fig. 14. Note, the mean prior β grain width is designated with letter 'd' to differentiate from the 'λ' used for the mean α lath width. Although the Hall-Petch relation can be seen for each individual data sets of RB and RP samples in the present work and this relation also holds true for the earlier work [10,12] where much smaller build heights (30 mm and 80 mm respectively) were used (the data are

presented in Fig. 14 for comparison), it is important to note that Hall-Petch relation simply does not provide a single good fitting when putting both data sets together (RB and RP samples). This suggests that the prior β grain width is not a good microstructural scale parameter that controls the mechanical properties in as-EBM Ti-6Al-4V. In the replotted prior β grain width result based on the work performed by Al-Bermani et al. [12], Fig. 14, the correlation coefficient of R^2=0.86 is found to be lower compared to that obtained for α lath width in Fig. 13 (R^2= 0.94). This seems to support the above-mentioned viewpoint. The discrepancies between the data in the present study and that of Al-Bermani etal. [12] and Tan et al. [10] could be also due to differences in chemistry of the powder used. The chemistry for RB and RP material are very similar (0.16 wt% Fe, 0.027 wt% N for RB and 0.17 wt% Fe, 0.029 wt% N for RP) but quite different from Al-Bermani et al. [12] (0.05 wt% Fe, 0.008 wt% N) and Tan et al. [10] (0.20 wt% Fe, 0.03 wt% N). The other factors are equipment type and EBM melting strategy (discussed in Section 4.1). Tan et al. [10] used Arcam A2XX equipment whereas the equipment used by Al-Bermani et al. [12] was Arcam S12 EBM machine which is an earlier generation of Arcam equipment. All these factors control the evolution of α lath width which in turn based on the above discussion can be considered as an important parameter for controlling the final mechanical properties.

5. Conclusions

A critical assessment on the graded microstructure and hardness in as-EBM Ti-6Al-4V round bar and rectangular plate samples was carried out. The following conclusions can be reached:

1. The different melting strategies do not change the Widmanstätten and lamellar α colony type of microstructure observed in EBM built Ti-6Al-4V alloy. However, they do result in different α lath widths that decrease with increasing the speed factor of the build strategy used.

2. An inhomogeneous graded microstructure with increase in prior β grain width and α lath width observed along the build direction is the consequence of decreasing cooling rate along the build.

3. The log-normal distribution of α lath width maps the big variation in α lath width distribution due to a small variation in temperature. The log-normal distribution gives the best fitting for the α lath width variation with build height.

4. The graded microstructure along the build has resulted in graded micro-hardness, higher and lower hardness at the bottom and top of the build respectively. The micro-hardness shows strong correlation with the mean α lath width and follows Hall-Petch relation. The α lath width instead of the prior β grain width is very likely to be primary microstructural scale parameter that controls the mechanical properties in as-EBM Ti-6Al-4V.

Acknowledgement

References

[1]   B. Dutta, F.H. Froes, Additive Manufacturing of Titanium Alloys, Adv. Mater. Process. 172 (2014) 18–23.

[2]   J.C.W. G. Lutjering, Titanium, 2nd ed., Springer, 2007.

[3]   C. Körner, Additive manufacturing of metallic components by selective electron beam melting — a review, Int. Mater. Rev. 61 (2016) 361–377.

[4]   U. Ackelid, M. Svensson, Additive manufacturing of dense metal parts by electron beam melting, Mater. Sci. Technol. Conf., (2009) 2711–2719.

[5]   W.E. Frazier, Metal additive manufacturing: A review, J. Mater. Eng. Perform. 23 (2014) 1917–1928.

[6]   E. Herderick, Additive manufacturing of metals: A review, Proc. Mater. Sci. Technol. Addit. Manuf. Met., Columbus, OH (2011).

[7]   D. Herzog, V. Seyda, E. Wycisk, C. Emmelmann, Additive manufacturing of metals, Acta Mater. 117 (2016) 371–392.

[8]   B. Wysocki, P. Maj, R. Sitek, J. Buhagiar, K. J. Kurzydłowski, W. Swieszkowski, Laser and electron beam additive manufacturing methods of fabricating titanium bone implants, Appl. Sci. 7 (2017) 657.

[9]   N. Hrabe, T. Gnäupel-Herold, T. Quinn, Fatigue properties of a titanium alloy (Ti–6Al–4V) fabricated via electron beam melting (EBM): effects of internal defects and residual stress, Int. J. Fatigue. 94 (2017) 202–210.

[10]   X. Tan, Y. Kok, Y.J. Tan, M. Descoins, D. Mangelinck, S.B. Tor, K.F. Leong, C.K. Chua, Graded microstructure and mechanical properties of additive manufactured Ti-6Al-4V via electron beam melting, Acta Mater. 97 (2015) 1–16.

[11]   A.A. Antonysamy, J. Meyer, P.B. Prangnell, Effect of build geometry on the β-grain structure and texture in additive manufacture of Ti-6Al-4V by selective electron beam melting, Mater. Charact. 84 (2013) 153–168.

[12]   S.S. Al-Bermani, M.L. Blackmore, W. Zhang, I. Todd, The origin of microstructural diversity, texture, and mechanical properties in electron beam melted Ti-6Al-4V, Metall. Mater. Trans. A. 41 (2010) 3422–3434.

[13]   A. Safdar, L.Y. Wei, A. Snis, Z. Lai, Evaluation of microstructural development in electron beam melted Ti-6Al-4V, Mater. Charact. 65 (2012) 8–15.

[14]   C. de Formanoir, S. Michotte, O. Rigo, L. Germain, S. Godet, Electron beam melted Ti–6Al–4V: Microstructure, texture and mechanical behavior of the as-built and heat-treated material, Mater. Sci. Eng. A. 652 (2016) 105–119.

[15]   X. Tan, Y. Kok, Y.J. Tan, G. Vastola, Q.X. Pei, G. Zhang, Y.W. Zhang, S.B. Tor, K.F. Leong, C.K. Chua, An experimental and simulation study on build thickness dependent microstructure for electron beam melted Ti–6Al–4V, J. Alloys Compd. 646 (2015) 303–309.

[16]   S.L. Lu, M. Qian, H.P. Tang, M. Yan, J. Wang, D.H. StJohn, Massive transformation in Ti-6Al-4V additively manufactured by selective electron beam melting, Acta Mater. 104 (2016) 303–311.

[17]   L.E. Murr, E. V. Esquivel, S.A. Quinones, S.M. Gaytan, M.I. Lopez, E.Y. Martinez, F. Medina, D.H. Hernandez, E. Martinez, J.L. Martinez, S.W. Stafford, D.K. Brown, T. Hoppe, W. Meyers, U. Lindhe, R.B. Wicker, Microstructures and mechanical properties of electron beam-rapid

manufactured Ti-6Al-4V biomedical prototypes compared to wrought Ti-6Al-4V, Mater. Charact. 60 (2009) 96–105.

[18] L. Ladani, Local and global mechanical behavior and microstructure of Ti-6Al-4V parts built using electron beam melting technology, Metall. Mater. Trans. A. 46 (2015) 3835–3841.

[19] S.L. Lu, H.P. Tang, Y.P. Ning, N. Liu, D.H. Stjohn, M. Qian, Microstructure and mechanical properties of long Ti- 6Al-4V rods additively manufactured by selective electron beam melting out of a deep powder bed and the effect of subsequent hot isostatic pressing, Metall. Mater. Trans. A. 46 (2015) 3824-3834.

[20] N. Hrabe, T. Quinn, Effects of processing on microstructure and mechanical properties of a titanium alloy (Ti-6Al-4V) fabricated using electron beam melting (EBM), part 1: Distance from build plate and part size, Mater. Sci. Eng. A. 573 (2013) 264–270.

[21] The Engineer UK, https://www.theengineer.co.uk/issues/june-2015-digi-issue/rolls-royce-breaks-additive-record-with-printed-trent-xwb-bearing/, June 2015.

[22] N. Raghavan, R. Dehoff, S. Pannala, S. Simunovic, M. Kirka, J. Turner, N. Carlson, S.S. Babu, Numerical modeling of heat-transfer and the influence of process parameters on tailoring the grain morphology of IN718 in electron beam additive manufacturing, Acta Mater. 112 (2016) 303–314.

[23] H. Helmer, A. Bauereiß, R.F. Singer, C. Körner, Grain structure evolution in Inconel 718 during selective electron beam melting, Mater. Sci. Eng. A. 668 (2016) 180–187.

[24] J. Dawes, R. Bowerman, R. Trepleton, Introduction to the additive manufacturing powder metallurgy supply chain, Johnson Matthey Technol. 59 (2015) 243–256.

[25] Arcam, Ti-6Al-4V Titanium Alloy, (2014) 4–6. doi:http://www.arcam.com/wp-content/uploads/Arcam-Ti6Al4V-Titanium-Alloy.pdf.

[26] ASTM F1472-14, Standard specification for wrought Ti-6Al-4V alloy for surgical implant applications (UNS R56400) (2015).

[27] C.A. Schneider, W.S. Rasband, K.W. Eliceiri, NIH Image to ImageJ: 25 years of image analysis, Nat. Methods. 9 (2012) 671.

[28] T. Searles, J. Tiley, A. Tanner, R. Williams, B. Rollins, E. Lee, S. Kar, R. Banerjee, H.L. Fraser, Rapid characterization of titanium microstructural features for specific modelling of mechanical properties, Meas. Sci. Technol. 16 (2005) 60–69.

[29] C. Qiu, N.J.E. Adkins, M.M. Attallah, Microstructure and tensile properties of selectively laser-melted and of HIPed laser-melted Ti-6Al-4V, Mater. Sci. Eng. A. 578 (2013) 230–239.

[30] C. He, P. Wang, M. Ling, S. Nai, J. Wei, Distribution of porosity in electron beam melting additive manufactured Ti-6Al-4V component, Ninth Pacific Rim Int. Conf. Adv. Mater. Process. (2016) 385–387.

[31] N. Hrabe, T. Quinn, Effects of processing on microstructure and mechanical properties of a titanium alloy (Ti-6Al-4V) fabricated using electron beam melting (EBM), part 2: Energy input, orientation, and location, Mater. Sci. Eng. A. 573 (2013) 271–277.

[32] B. Cheng, S. Price, J. Lydon, K. Cooper, K. Chou, On process temperature in powder-bed electron beam additive manufacturing: model development and validation, J. Manuf. Sci. Eng. 136 (2014) 061018.

[33] N. Shen, K. Chou, Thermal modeling of electron beam additive manufacturing process - powder sintering effects, Proceedings of the ASME 2012 International Manufacturing Science and Engineering Conference (2016) 1–9.

[34] E. Lee, R. Banerjee, S. Kar, D. Bhattacharyya, H.L. Fraser, Selection of a variants during microstructural evolution in α/β titanium alloys, Philos. Mag. 87 (2007) 3615–3627.

[35] D. A. Porter, K. E. Esterling, M.Y. Sherif, Phase transformations in metals and alloys, 2009.

[36] H.S. Carslaw and J.C. Jaeger, Conduction of heat in solids, Oxford University Press, London, 1959.

[37] S.L. Semiatin, S.L. Knisley, P.N. Fagin, F. Zhang, D.R. Barker, Microstructure evolution during alpha-beta heat treatment of Ti-6Al-4V 34 (2003) 8–10.

[38] R.W. Armstrong, Engineering science aspects of the hall-petch relation, Acta Mech. 225 (2014) 1013–1028.